

Geophysical Research Letters

RESEARCH LETTER

10.1029/2019GL085408

Key Points:

- This is the so-far largest earthquake in a salt-mining area where seismicity has been increased in previous 10 years by injection-induced events
- Mainshock nucleated as a thrust, then rupturing a previously unknown strike-slip fault, suboptimally oriented to regional stress field
- The complex nature of the event explains its small double-couple component and diversity of focal mechanisms across reporting agencies

Supporting Information:

- Supporting Information S1

Correspondence to:

J. Liu,
woxin5295@yahoo.com

Citation:

Liu, J., & Zahradnik, J.. (2020). The 2019 M_W 5.7 Changning earthquake, Sichuan Basin, China: A shallow doublet with different faulting styles. *Geophysical Research Letters*, 47, e2019GL085408. <https://doi.org/10.1029/2019GL085408>

Received 14 SEP 2019

Accepted 5 FEB 2020

Accepted article online 24 MAR 2018

The 2019 M_W 5.7 Changning Earthquake, Sichuan Basin, China: A Shallow Doublet With Different Faulting Styles

Junqing Liu¹  and Jiří Zahradník² 

¹Jilin Earthquake Agency, China Earthquake Administration, Changchun, China, ²Faculty of Mathematics and Physics, Charles University, Prague, Czech Republic

Abstract The increased seismic activity of the last ~10 years in Changning county of Sichuan Province comprised just small (mostly $M_L < 5.0$) injection-induced earthquakes. The M_W 5.7 earthquake on June 17, 2019, is the largest event ever reported there. Moment tensor of the mainshock was remarkably dominated by a compensated linear vector dipole. We resolve its fine structure showing it was a doublet, allowing approximation by a thrust- and strike-slip subevent. The mainshock nucleated as thrust faulting, which (together with the largest aftershocks) can be linked with previously known reverse faults, favorably oriented to regional stress field. Contrarily, the strike-slip segment of the mainshock, less favorably oriented, was probably facilitated by elevated pore pressure due to previous injections. Shallow active strike-slip faulting, not yet mapped in the region, is a new feature, important for future hazard assessment.

Plain Language Summary Changning county in Sichuan Basin belongs to major salt-producing resources, with water injection wells drilled to ~3-km depths. Enhanced occurrence of small earthquakes was observed in the last ~10 years. However, on June 17, 2019, a damaging earthquake struck the region. Seismic agencies reported diverse focal mechanisms and pointed to departures from shear faulting, typical for tectonic events. To understand these enigmatic features, we modeled records from 12 broadband seismic stations, adding over 100 first-motion polarities. We found that the earthquake was very shallow (~4 km) and consisted of two shear events: the initial thrust faulting and the following strike-slip faulting along an SE-NW trending near-vertical plane, aligned with aftershocks. The initial episode was “normal,” expected on existing faults and supported by tectonic stresses of the region. Contrarily, the significant strike-slip faulting appears to be rather “abnormal,” probably facilitated by the initial shock and by elevated pressure of underground fluids. The 2019 earthquake provided a rare opportunity to illuminate interplay between long-lasting water injections, tectonic stress, complexity of existing faults, and their dynamic interactions. That is how seismology aims at making industrial activities sustainable and safe.

1. Introduction

Earthquake doublets provide clues for understanding complex fault systems (e.g., Danré et al., 2019; Hicks & Rietbrock, 2015; Lay et al., 2013). Particularly challenging are closely spaced doublets whose subevents have unequal focal mechanisms, separated just by a few kilometers and a few seconds, intuitively suggesting a causal relationship between the involved faults. Global low-frequency moment tensor (MT) solutions provide only an overall characterization of such events, often featuring large non-double-couple (non-DC) components. This paper makes use of superior quality of broadband Chinese seismic networks and reveals one such a rare closely spaced doublet in a salt-mining district of Sichuan Basin. It points to the existence of segmented faulting, especially to an unmapped shallow strike-slip (SS) fault, important for future seismic hazard assessment in this densely populated region of the world.

Sichuan Basin belongs to major gas and oil resources in China. The annual natural gas production should be as high as $5 \times 1,010 \text{ m}^3$ in 2030 (Ma, 2017). The basin, important also for its agriculture, supports a population of over 100 million. Three shale-gas fields in the southern part of the basin, Shangluo, Zhaotong, and Changning, were reported as sites of induced seismic events (Lei et al., 2017, 2019a; Meng et al., 2019). The Sichuan Basin also belongs to the main salt-producing areas, using the solution mining method, with injection wells drilled to ~3-km depths. Increased seismicity has been recognized in the last ~10 years, likely related to the long-lasting water injection in the Changning salt mines (Sun et al., 2017). Given that

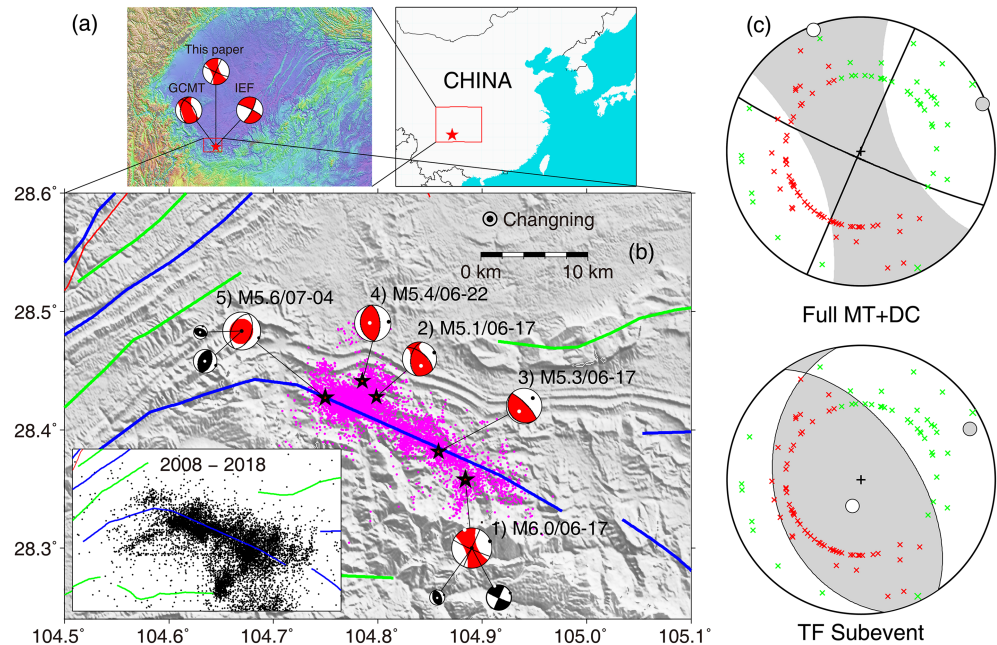


Figure 1. The 2019 Changning earthquake sequence. (a) Sichuan Basin, China. Focal mechanism of the mainshock, provided by two agencies (GCMT and IEF) and this paper. (b) The mainshock (M 6.0) and four M 5+ aftershocks are shown by stars and the focal mechanism symbols; the smaller aftershocks are plotted as pink points. The earthquakes were relocated in this paper using the CENC phase data and HypoDD method (Waldhauser & Ellsworth, 2000). For the two largest shocks, most deviating from a double-couple (DC) model, their focal mechanism diagram is split in two: the major and minor DC. Major tectonic elements are plotted as lines: anticlines (blue), synclines (green), and the known active faults (red). Inset in panel (b) demonstrates the previous 10-year activity of the region, $M > 0$ (CENC). (c) The first-motion polarities of the mainshock (compressions in red and dilatations in green) clearly disagree with the full-MT solution, but they are very well explained by the thrust-fault nucleation subevent; the diagrams in panel (c) are not scaled with the moment.

potential seismogenic faults are poorly known, events of magnitude greater than 6.0 cannot be ruled out (Lei et al., 2019a).

Indeed, on June 17, 2019, according to the China Earthquake Networks Center (CENC), an M 6.0 earthquake occurred in Changning county (see Figure 1). Hereafter, according to current practice in China, we use a generic symbol M , denoting either local magnitude M_L or an empirical estimate of the surface-wave magnitude $M_S = 1.13, M_L - 1.08$ (Chen et al., 2014), for events below or above $M_L \sim 5$, respectively. The earthquake killed 13 people. More than 200 were injured, and a large number of buildings were damaged (Yi et al., 2019). This is another $M > 5.0$ earthquake occurring in 2019 in the Gongxian-Changning region, Sichuan Province, after the M_L 5.3 earthquake on January 3, 2019, studied by Lei et al. (2019a). Only nine $M \geq 5.0$ earthquakes have been previously known to occur in the Changning and adjacent areas: Yibin M 5.5 in 26 BC, Gaoxian M 5.5 in 1610, Nanxi M 5.0 in 1892, Zigong M 5.7 in 1896, Weiyuan M 5.0 in 1905, Jiangan M 5.0 in 1936, Zigong M 5.0 in 1954, Fushun M 5.0 in 1959, and Yibin M 5.4 in 1996 (China Earthquake Administration, 1995).

The June 17, 2019, M 6.0 earthquake occurred at a distance of a few kilometers from the salt-mining wells (Lei et al., 2019b). The mainshock was followed by an aftershock sequence, including four M 5+ events, forming a clear line (subvertical planar) structure, ~ 20 km long, trending southeast-northwest (Figure 1b). This trend coincides with the major tectonic element of the area, the Changning anticline. There are many small faults in the anticlinal structure, often associated with a typical caprock/fold system, most of them being reverse faults (Qian & Tang, 1992; Sun et al., 2017).

The 2019 M 6.0 event is noteworthy for a very large compensated-linear-vector-dipole (CLVD) component of its single-point source model; for example, Global Centroid Moment Tensor (GCMT) Project reported the CLVD of -98% . Later, in the paper, we demonstrate that this significant non-DC character of the event may explain great scatter between the strike/dip/rake angles reported by several agencies, for example,

thrust faulting (TF) of GCMT and SS of Institute of Earthquake Forecasting (IEF, China Earthquake Administration), shown in Figure 1a. It also explains why first-motion polarities do not fit with the full MT; see Figure 1c (top).

While the contemporary evidence that injection can cause earthquakes is undoubted (Ellsworth, 2013; Grigoli et al., 2018), very little is known about relatively large earthquakes occurring in regions previously activated by injection activities and thus far experiencing only smaller events. How is their rupture nucleating, propagating, and eventually causing aftershocks? Therefore, we focus on the source process of the M 6.0 event and its M 5+ aftershocks. We resolve spatiotemporal complexity of the mainshock and causative faults. Finally, we demonstrate that the SS segment of the mainshock is suboptimally oriented to the regional stress field, indicating possible pore pressure effects.

2. Source Models of the Mainshock

Our waveform data of the M 6.0 mainshock consist of 12 broadband records at epicentral distances \sim 120–210 km (see Figure S1 in the supporting information). The station selection was based on data quality (low noise and absence of disturbances; Zahradník & Plešinger, 2010) and azimuthal coverage. Several velocity models were tested, providing qualitatively the same results, for example, Crust 2.0 (Bassin et al., 2000). The waveform modeling is performed with established methods (Sokos et al., 2015, 2016; Zahradník et al., 2017) and recently developed uncertainty assessments, detailed in Text S1.

The single-point source models pointed to a highly non-DC solution. A typical full MT is presented for the range of 0.03–0.06 Hz in Figure 1 and Tables S1 and S2. Without loss of generality, hereafter, we demonstrate results for a regional velocity model (Zhao & Zhang, 1987), shown in Table S3, the same model as used by Sun et al. (2017). The centroid depth is definitely very shallow, 3–5 km. In this depth range, the DC part of the full MT is low (\sim 10%), and it varies from TF to SS faulting (see Figures 2a and S2). The formally best-fit solution is found at the depth of 4 km, consisting of DC = 20%, CLVD = -68% , and ISO = -12% . The GCMT solution was similar in terms of its high negative CLVD percentage (-98%) but placed the event much deeper at 12 km. The waveform fit of our model is very good (variance reduction [VR] = 0.90, Figure S1a). A formal decomposition of MT into two DC parts (Jost & Herrmann, 1989) yields the moment ratio of the minor DC to major DC equal 0.61, with strike/dip/rake angles (hereafter s/d/r, in degrees) = 336/48/86 and 114/86/ -1 , respectively.

At shallow depths and relatively low frequencies, the MT resolution is limited and must be accompanied by an assessment of uncertainties and parameter trade-offs (Halló et al., 2017, 2019; Vackář et al., 2017). Using these new methods, validated also on nuclear tests (Liu, Li, Zahradník, Sokos, & Plicka, 2018; Liu, Li, Zahradník, Sokos, Liu, & Tian, 2018) and demonstrated in Figure 2b, we find that nodal planes are strongly nonunique. While the P -axis is very well resolved (P_{azimuth} 69°, P_{plunge} 3°), the T -axis is arbitrary in the orthogonal plane. Well resolved also are the ISO percentage (almost vanishing), the large negative CLVD%, and the low DC%. The event is basically a CLVD whose major axis, almost horizontal, is the only axis well resolved (Figure S3).

Extending the frequency range of the waveform inversion, the source appears to be composed of several subevents. Here we present a typical example of the results for the frequency range of 0.03–0.10 Hz; a further increase would deteriorate waveform fit due to the inherent inaccuracy of the velocity model. In this extended range, the single-point full-MT solution decreases VR from 0.90 to 0.80, due to increased complexity of waveforms (Figures S1a and S1b). Assuming that the rupture process might have included several tectonic faults, we focus on seeking subevents in DC-constrained mode. After experimentation with various geometries of the trial source grids, we present multiple-point source models for a horizontal line grid at a depth of 4 km (Figure 3). We choose azimuth of 120°, close to the aftershock alignment. Similar results were obtained for a line deepening from 2.4 to 6.1 km in the northwestern direction. Using iterative deconvolution (Zahradník & Sokos, 2018), the model suggests two subevents (Figure 3a): a dominant SS, slightly NW shifted relative to the epicenter, and a weaker thrust fault, shifted to SE. Their moment ratio TF/SS is low, \sim 0.35. Perturbing the parameters (e.g., the line azimuth, grid increment, or frequency), the space-time separation and size of the subevents are varying. However, the two focal mechanisms remain very stable (Table S1), close to the formal major/minor DC components of the single-point source model. Another strong indication of the stability is provided by the modified iterative deconvolution in which the moment release is artificially “slowed down,” providing models closer to finite-fault slip inversions (Zahradník &

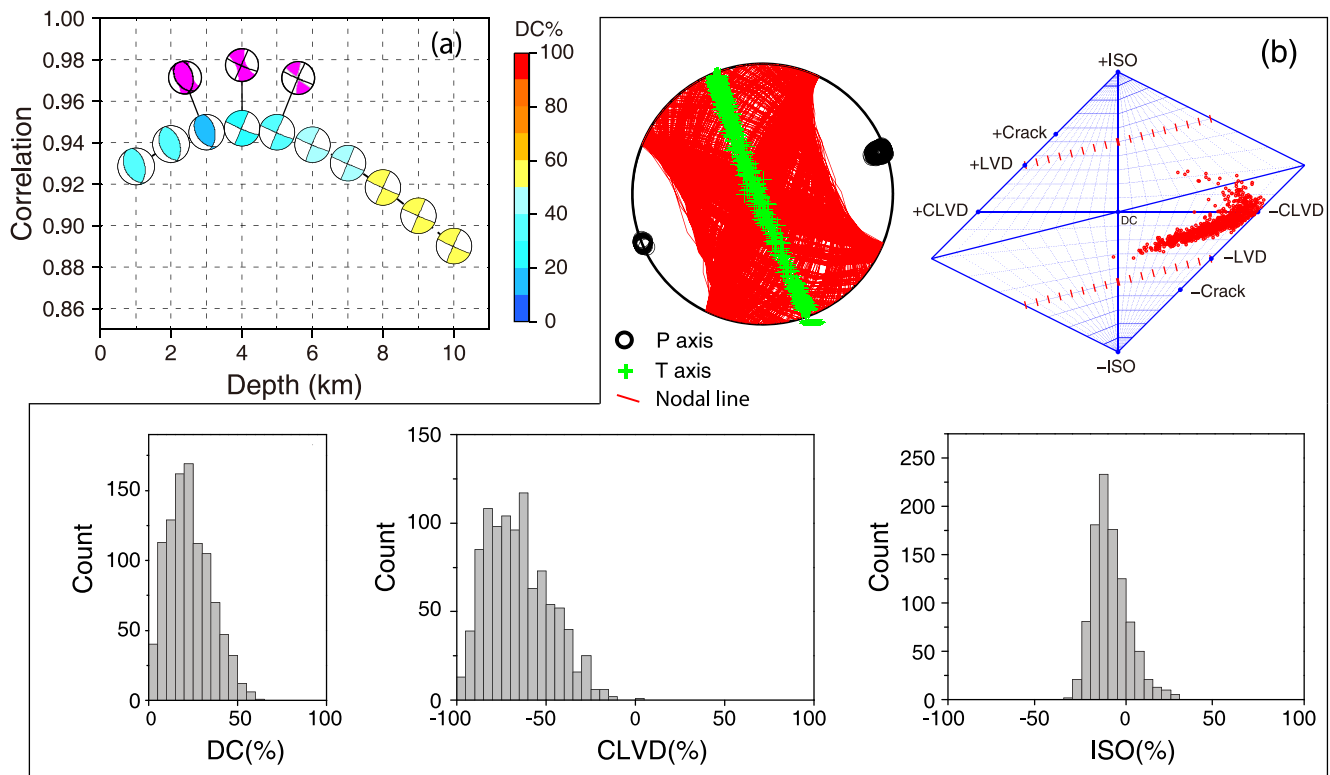


Figure 2. Single-point source analysis of the mainshock (0.03–0.06 Hz). (a) Correlation between observed and synthetic waveforms versus depth. The DC focal mechanism symbols (depth of 1–10 km) are color coded relative to the DC percentage. Shown for the depth of 3–5 km is also the full moment tensor. (b) Uncertainty shown by random sampling of the posterior probability density of model parameters (nodal lines and P-T axes, the source-type plot (Hudson et al., 1989), and histograms of the DC, CLVD, and ISO). Due to shallow depth and the remarkably non-DC character, only the *P*-axis is resolvable. It demonstrates a limited physical meaning of the single-point low-frequency models, if presented without uncertainties.

Gallovič, 2010). Although the DC-constrained focal mechanisms are free for all calculated subevents, we again obtain just two source types: the SS and TF (Figure 3b). Here, in Figure 3b, the TF rupture again appears earlier than SS, shifted to SE, but the moment ratio TF/SS is larger, ~ 1.2 .

The best insight into space-time separation and moment ratios of subevents is provided by a joint search for the TF-SS source pairs (Zahradník & Sokos, 2014), using non-negative least squares (Lawson & Hanson, 1974). Here (Figures 3c–3e) we fix the *s/d/r* angles of the subevents and use frequency 0.03–0.10 Hz, as above. Twelve of the two-point DC-constrained models shown in Figure 3c have $VR > 0.80$, greater than the single-point full-MT solution. A stable feature is the position of the SS event, preferred in points 7 to and 9, and the significant involvement of the thrust-fault subevent: The moment ratio of the TF/SS subevents varies from 0.3 to 1.2. Their tensor sum yields CLVD between -46% and -90% , in good agreement with low-frequency single-point full-MT model (Table S1). An exact thrust-fault subevent position and its timing are not unambiguously resolved (Figures 3d and S4). Nevertheless, most likely, the SS subevent is delayed and northwestward shifted ~ 3 – 9 km relative to the TF subevent. The TF subevent can be situated at the hypocenter (point 7). The formally best-fitting two-point model is the pair (SS,TF) with position (8,6), characterized by $VR = 0.84$. Its TF/SS moment ratio is 0.72, the subevent separation of 6 km, and the moment-rate function (Figure 3e) indicates a 2-s time delay of SS relative to TF. If considering just the SS subevent of this pair, VR would drop to 0.72 (Figure S1d).

To prove that the mainshock source process started with TF, we employ independent information about the initial (nucleation) part of the source process, provided by first-motion polarities. We visually inspected more than 120 stations and kept the 109 most reliable readings (Figures 1c and S5). These polarities have been projected onto focal sphere using the same velocity model as in the waveform inversion, with several trial depths. For an arbitrary depth between 3 and 5 km, the observed polarities are well fitted with the TF mechanism. At the same time, neither the SS mechanism nor the full-MT single-point model can

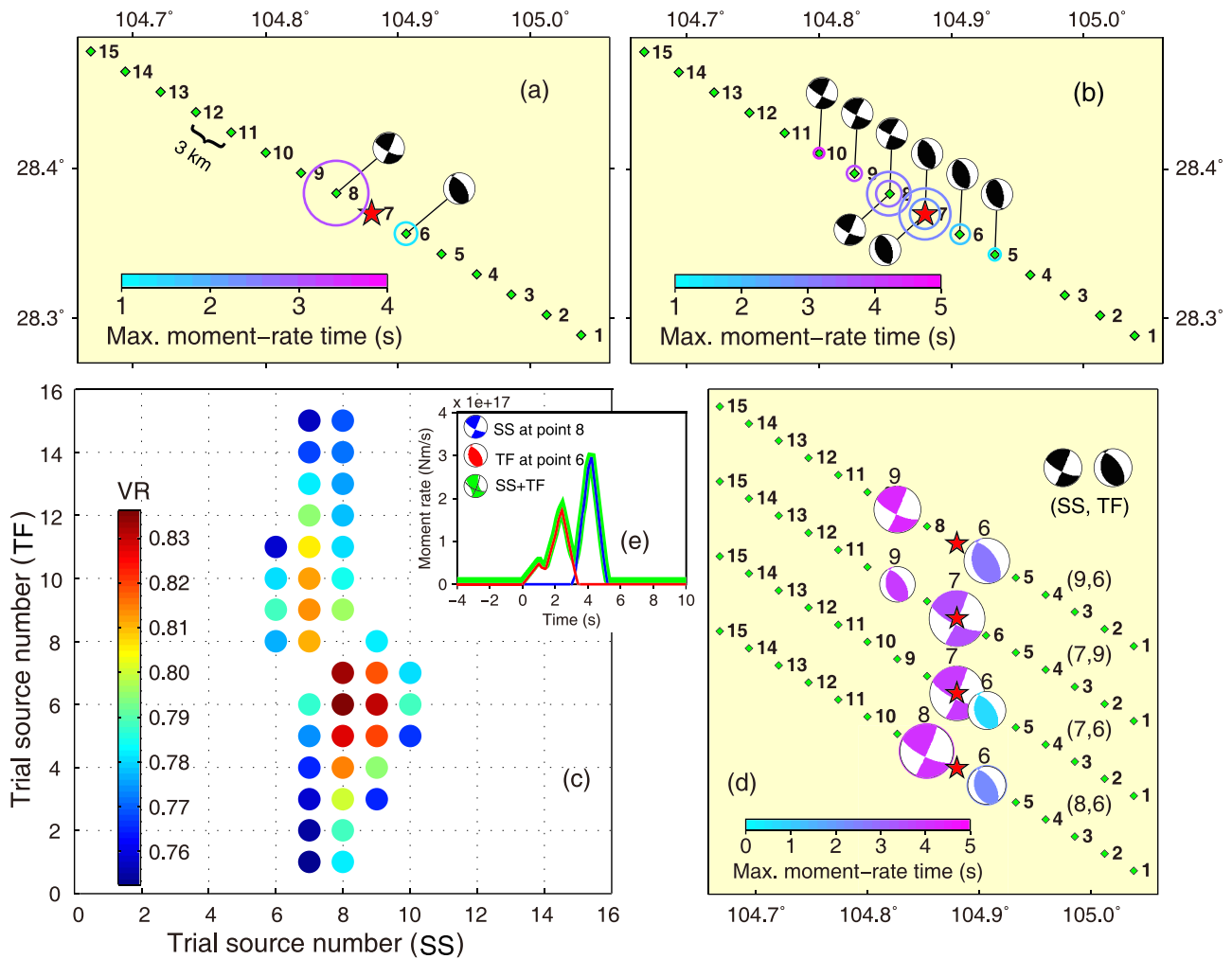


Figure 3. Multiple-point source modeling of the mainshock on a horizontal line grid by three methods (depth of 4 km, 0.03–0.10 Hz). The trial source points are shown by diamonds 1–15; the epicenter is shown by a star. Subevents (open circles) are color coded relative to time and sized according to the moment. The modeling methods include (a) iterative deconvolution—two subevents with free DC-constrained moment tensors; (b) modified iterative deconvolution—eight subevents with free DC-constrained moment tensors; and (c) joint inversion for source pairs, each one consisting of an SS and TF subevent, whose DC focal mechanisms were prescribed. The source pairs fitting data almost equally well are shown by small filled circles, colored relative to their waveform fit (variance reduction [VR]); the horizontal and vertical axes refer to the position of the SS and TF subevent, respectively. (d) Four examples of the DC source pairs on the same line as in panel (a), formally shifted for the presentation, color coded relative to time, and circle sized according to moment. (e) The moment-rate time function for the best-fitting source pair (8,6) with the moment ratio TF/SS = 0.72, CLVD = –83%, VR = 0.84. The blue and red lines refer to SS and TF, respectively; the sum is shown in green. For more details, see Figure S4. The mainshock undoubtedly comprised both the thrust- and strike-slip faulting.

explain the data. Worth to mention that if directly inverting the polarities (without any waveform inversion), using FOCMEC code (Snoko, 2003), we obtain a mechanism just negligibly deviating from our TF, Kagan angle $<20^\circ$ (see Figure S6). Therefore, we conclude that the mainshock was a closely spaced TF + SS doublet, nucleating as a thrust. The term “doublet” accentuates the two involved focal mechanisms rather than two distinct episodes. Our approximate model does not rule out a possibly continuous source process.

3. Discussion

The mainshock M 6.0 was followed in 41 minutes by an M 5.1 aftershock, shifted ~ 10 km to NW. Then, 8 hours later, an M 5.3 occurred close to the largest shock. Finally, 5 and 17 days later, the M 5.4 and M 5.6 aftershocks, respectively, appeared northwestward of the M 5.1; see Figure 1b. The earthquakes were “jumping forth and back” in the SE–NW direction along the mapped anticline. Most of the observed smaller aftershocks followed the same trend (also Figure 1b), without any systematic space–time migration, perhaps except the dominance of the latest events at NW (Figure S7). We have shown that significant perhaps

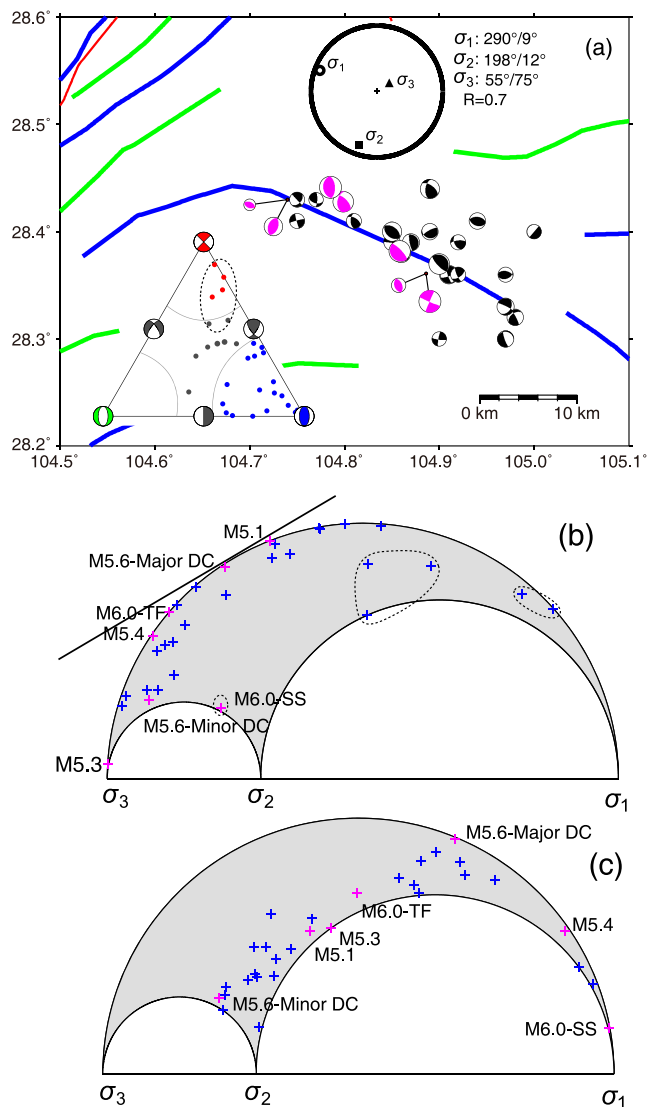


Figure 4. The pre-2019 stress field and resolved tractions. (a) Focal mechanisms studied in this paper (pink) and others (black); the latter include eight events of 2019 and 16 older ones, 2006–2015, all $M > 3.6$, taken from literature (Liu et al., 2019; Ran et al., 2008; Wang et al., 2015; Yi et al., 2019; Zhu & He, 2014). The upper inset shows the pre-2019 regional stress field (Liu et al., 2019)—the principal axes (azimuth/plunge) and the shape ratio R . Faults as in Figure 1. The bottom inset is a ternary diagram (Frohlich, 1992). (b) The events of panel (a) are displayed on Mohr's diagram, using their nodal planes of the greater shear instability. The shear and normal tractions correspond to the vertical and horizontal coordinates, respectively. The fracture criterion for the friction coefficient of 0.6 is shown by the tangent line. (c) The same events as in panel (b) but using the more stable nodal planes. Note that the stress field is not calculated here. Focal mechanisms serve just for resolving tractions in the a priori known stress field. It is inferred that the left-lateral SS subevent of mainshock (M 6.0-SS) belongs to a few earthquakes that are most distant from the tangent line, that is, the least favorably oriented to the stress field. Those six events are depicted by the dotted ovals, and all of them are SSs or very close to SS mechanism (red dots in the ternary diagram). Their fractures could be assisted by the pore pressure diffusion due to water injection activities of the previous years (Sun et al., 2017).

even dominant part of the mainshock was an SS subevent, whose one nodal plane (strike $\sim 120^\circ$) agrees with this NW-SE structure. Therefore, we suggest that the mainshock included an unmapped left-lateral SS, aligned with the mapped anticline structure. The GCMT solution (Figure 1a) does not indicate an SS faulting geometry in the best-DC nodal lines. Nevertheless, a formal decomposition of the GCMT solution into the major and minor DC parts does provide an almost same SS and TF mechanisms as found in this paper, with the TF/SS moment ratio of 1.04. Note however that our physically based retrieval of the two subevents is deeper than the formal decomposition. Besides the SE-NW trend, the aftershock distribution indicated also shorter faults, for example, an N-S trending structure, seen in Figure 1b near the M 6.0 epicenter.

Seismic activity parallel with the anticline has been well documented by the 2008–2018 seismicity (Figure 1b, inset). In Sichuan Basin we face a caprock/fold system in the uppermost 3–6 km, slowly slipping on the underlying basement (a “decoupling” process). The anticlines of the caprock/fold are rich in symbiotic faults, whose majority are steeply dipping thrust faults, and earthquakes often occur on such faults inside the caprock (Qian & Tang, 1992). This is consistent with the observed event depths in our study (Table S1); except one M 5+, the events are shallower than 5 km. However, the cited authors also claimed that the caprock/fold system cannot accumulate a large amount of strain, which contrasts with the relatively large magnitude of the 2019 earthquake.

A closer look at the 10-year seismicity reveals some deviations from the general SE-NW seismicity trend. It points to a complex system of active faults, also indicated by deviatoric focal mechanisms of the M 5+ events (Figure 1, Table S1), whose nodal planes are not parallel with the NW-SE anticline. Three TF mechanisms have a very high DC percentage. All these mechanisms share similar azimuth of the P -axis as the mainshock, 47 – 84° . This finding is in agreement with geological evidence that the shale and sandstone rocks of the anticline include small faults whose majority are thrust faults (Sun et al., 2017). In this sense, we interpret the TF nucleation of the mainshock as an expected rupture process.

According to our MT analysis, one of the M 5+ aftershocks is different (M 5.6 in Figure 1b and Table S1). It is the most delayed and the deepest one, occurring on July 4, near the NW termination of the supposed mainshock rupture. This M 5.6 TF event has again a significant non-DC character, but, opposed to the mainshock, its CLVD is positive ($\sim 80\%$). As such, its formal major/minor DC decomposition shares a common T -axis, and both DC parts are thrust faults (Figure 1b). Due to smaller magnitude, this event is more challenging than the mainshock; thus, we cannot prove whether it actually consisted of two subevents or not. The event should deserve more attention elsewhere, possibly illuminating the region where the major anticline is changing from linear to a bended structure. Not only such a bend could have stopped the mainshock rupture, but also it might be generally less active as suggested by the 2008–2018 activity in Figure 1b (inset).

Finally, in Figure 4, we compare the 2019 sequence with the regional stress field. The stress was calculated from 39 focal mechanisms of 2008–2016 (Liu et al., 2019). Using the given stress, similarly as Hainzl et al. (2016), we resolve shear and normal tractions on both nodal planes and identify the planes with greater shear instability (defined by

Vavryčuk, 2014). Importantly, the SS subevent of the mainshock (M 6.0-SS) belongs to a few six events, all of the SS type, least susceptible to failure (most distant from the Mohr's circle envelope), that is, less favorably oriented to the stress. Thus, we recall the water injection effects of the previous years (Sun et al., 2017) and suggest that the SS component of the mainshock was likely facilitated by the elevated pore pressure. Additional effects, for example, poroelastic coupling and time-dependent nucleation (Segall & Lu, 2015), would require specific modeling that is beyond the scope of the present paper. Static Coulomb stress perturbation caused by TF fault, allowing rupture of SS fault, is inconclusive (Figure S8). Due to the space-time proximity of the two subevents, a likely scenario appears to be a continuous evolution of a single stress-fluid-fault system, involving two segments of different faulting styles. From the longer-term perspective, the 2019 earthquake sequence might have been affected by the M 5.7 Xingwen earthquake (December 18, 2018, 28.24°N, 104.95°E), thought to be induced by hydraulic fracturing in the southerly adjacent Shangluo shale gas area (Lei et al., 2019b).

4. Conclusions

The Changning county in Sichuan Basin, China, has been known for the frequent occurrence of small ($M_L < 5$) injection-induced seismic events, particularly well documented in the 2008–2018 period. Generally, earthquakes follow a major tectonic element—the SE-NW trending anticline. The anticline is a caprock/fold system, 3–6 km thick, slowly slipping on the underlying basement. The earthquakes occur inside this depth range. The system was considered unable to accumulate large strains, but the recent 2019 M_W 5.7 (M 6.0) event indicates that moderate earthquakes are possible.

We analyzed MTs of the mainshock and all major (M 5.1–5.6) aftershocks, finding shallow centroid depths and various focal mechanisms. The aftershocks appeared to be basically thrust faults. This finding is consistent with previous studies that declared small thrusts to be typical for the region. The mainshock was composed of two subevents: TF and SS. This complex faulting geometry caused the notable non-DC character of the single-point low-frequency source models and explains why focal mechanisms varied among several reporting agencies. The significant left-lateral SS subevent, striking parallel with the anticline and aftershocks, is a new finding. Long seismically active SS faults have not been mapped in the region yet and should be considered in the seismic hazard assessment.

The mainshock nucleated as a thrust fault, well oriented to the regional stress field. Then, within a few seconds and a few kilometers, it progressed toward the northwest as an SS rupture. The SS faulting, less favorably oriented to regional stress than TF, was probably facilitated by the elevated pore pressure due to previous water injections. The adopted two-point model is an approximation of a possibly continuous rupture process, involving a smooth transition between the TF and SS segments. A deeper insight into the observed fault-stress-fluid interactions would require extensive finite-source dynamic modeling (Galis et al., 2017; Gallovič et al., 2019).

References

- Basson, C., Laske, G., & Masters, G. (2000). The current limits of resolution for surface wave tomography in North America. *EOS, Transactions American Geophysical Union*, 81, F897.
- Chen, Z., Chen, H., Zhao, C., Wang, Q., Hua, W., & Zhou, L. (2014). Measurement of Earthquake Size. *Earthquake Research in China*, 28(3), 285–298.
- China Earthquake Administration. (1995). *The catalogue of Chinese historical strong earthquakes*. Beijing: Seismological Press.
- Danré, P., Yin, J., Lipovsky, B. P., & Denolle, M. A. (2019). Earthquakes within earthquakes: Patterns in rupture complexity. *Geophysical Research Letters*, 46, 7352–7360. <https://doi.org/10.1029/2019GL083093>
- Ellsworth, W. L. (2013). Injection-induced earthquakes. *Science*, 341, 1225942. <https://doi.org/10.1126/science.1225942>
- Frohlich, C. (1992). Triangle diagrams: Ternary graphs to display similarity and diversity of earthquake focal mechanisms. *Physics of the Earth and Planetary Interiors*, 75(1–3), 193–198. [https://doi.org/10.1016/0031-9201\(92\)90130-N](https://doi.org/10.1016/0031-9201(92)90130-N)
- Galis, M., Ampuero, J. P., Mai, P. M., & Cappa, F. (2017). Induced seismicity provides insight into why earthquake ruptures stop. *Science Advances*, 3(12), eaap7528. <https://doi.org/10.1126/sciadv.aap7528>
- Gallovič, F., Valentová, L., Ampuero, J. -P., & Gabriel, A. -A. (2019). Bayesian dynamic finite-fault inversion: 1. Method and synthetic test. *Journal of Geophysical Research: Solid Earth*, 124, 6949–6969. <https://doi.org/10.1029/2019jb017510>
- Grigoli, F., Cesca, S., Rinaldi, A. P., Manconi, A., López-Comino, J. A., Clinton, J. F., et al. (2018). The November 2017 M_W 5.5 Pohang earthquake: A possible case of induced seismicity in South Korea. *Science*, 360(6392), 1003–1006. <https://doi.org/10.1126/science.aat2010>
- Hainzl, S., Fischer, T., Čermáková, H., Bachura, M., & Vlček, J. (2016). Aftershocks triggered by fluid intrusion: Evidence for the aftershock sequence occurred 2014 in West Bohemia/Vogtland. *Journal of Geophysical Research: Solid Earth*, 121, 2575–2590. <https://doi.org/10.1002/2015JB012582>

Acknowledgments

Regional waveform data for this study were taken from the data repository of the China Seismic Experimental Site (2019). Wave 6.1. CSES Scientific Products, doi:10.12093/01db.01.2019.03.v1. The 2008–2018 seismicity and phase data of the 2019 aftershocks were taken from the repository of CENC, <http://www.ceic.ac.cn/history>. Tectonic lines and topography were drawn according to <http://www.cses.ac.cn/?cat=133> and <http://srtm.csi.cgiar.org/>, respectively. We used also the Coulomb 3 code, <https://earthquake.usgs.gov/research/software/>. Figures were partly created using GMT 4.5.16 (<http://gmt.soest.hawaii.edu/home>). Codes for the major/minor DC decomposition and for ternary diagram, written by M. Halló, were used (<http://geo.mff.cuni.cz/~hallo/>). The Stressinverse code (Vavryčuk, 2014) was modified for Figure 4 by one of the authors of this paper (J. Z.). Software ISOLA (developed by J. Z. and E. Sokos) was used and can be downloaded with the latest updates from http://geo.mff.cuni.cz/~jz/for_Cuba2018/. J. L. was supported by the National Natural Science Foundation of China Grants 41474114 and 41874125. J. Z. was supported by the Czech Science Foundation Grant GAČR-18-06716J. We thank J. Ritsema (editor), the two reviewers (H. AgurtoDetzel and anonymous), and F. Gallovič for the insightful comments.

- Halló, M., Asano, K., & Gallovič, F. (2017). Bayesian inference and interpretation of centroid moment tensors of the 2016 Kumamoto earthquake sequence, Kyushu, Japan. *Earth, Planets and Space*, 69, 134. <https://doi.org/10.1186/s40623-017-0721-4>
- Halló, M., Opršal, I., Asano, K., & Gallovič, F. (2019). Seismotectonics of the 2018 northern Osaka M6.1 earthquake and its aftershocks: Joint movements on strike-slip and reverse faults in inland Japan. *Earth, Planets and Space*, 71, 34. <https://doi.org/10.1186/s40623-019-1016-8>
- Hicks, S. P., & Rietbrock, A. (2015). Seismic slip on an upper-plate normal fault during a large subduction megathrust rupture. *Nature Geoscience*, 8(12), 955–960. <https://doi.org/10.1038/ngeo2585>
- Hudson, J. A., Pearce, R. G., & Rogers, R. M. (1989). Source type plot for inversion of the moment tensor. *Journal of Geophysical Research*, 94(B1), 765–774. <https://doi.org/10.1029/JB094iB01p00765>
- Jost, M. L., & Herrmann, R. B. (1989). A student's guide to and review of moment tensors. *Seismological Research Letters*, 60(2), 37–57. <https://doi.org/10.1785/gssrl.60.2.37>
- Lawson, C., & Hanson, R. (1974). *Solving least squares problems*. Upper Saddle River, NJ: Prentice-Hall.
- Lay, T., Duputel, Z., Ye, L., & Kanamori, H. (2013). Interactions between near-trench intraplate thrust and normal faulting. *Physics of the Earth and Planetary Interiors*, 220, 73–78. <https://doi.org/10.1016/j.pepi.2013.04.009>
- Lei, X., Huang, D., Su, J., Jiang, G., Wang, X., & Wang, H. (2017). Fault reactivation and earthquakes with magnitudes of up to M_w 4.7 induced by shale-gas hydraulic fracturing in Sichuan Basin, China. *Scientific Reports*, 7, 7971. <https://doi.org/10.1038/s41598-017-08557-y>
- Lei, X., Wang, Z., & Su, J. (2019a). The December 2018 M_L 5.7 and January 2019 M_L 5.3 earthquakes in South Sichuan Basin induced by shale gas hydraulic fracturing. *Seismological Research Letters*, 90(3), 1099–1110. <https://doi.org/10.1785/0220190029>
- Lei, X., Wang, Z., & Su, J. (2019b). Possible link between long-term and short-term water injections and earthquakes in salt mine and shale gas site in Changning, South Sichuan Basin, China. *Earth and Planetary Physics*, 3(6), 510–525. <https://doi.org/10.26464/epp2019052>
- Liu, J., Li, L., Zahradník, J., Sokos, E., Liu, C., & Tian, X. (2018). North Korea's 2017 test and its non-tectonic aftershock. *Geophysical Research Letters*, 45, 3017–3025. <https://doi.org/10.1002/2018GL077095>
- Liu, J., Li, L., Zahradník, J., Sokos, E., & Plicka, V. (2018). Generalized source model of the North Korea tests 2009–2017. *Seismological Research Letters*, 89(6), 2166–2173. <https://doi.org/10.1785/0220180106>
- Liu, J., Wan, Y., Huang, Z., Li, Z., Hu, X., & Li, Z. (2019). Study on central focal mechanism of the Changning M6.0 earthquake in Sichuan and tectonic stress field around the earthquake. *Technology for Earthquake Disaster Prevention*, 14(3), 678–686. <https://doi.org/10.11899/zzfy20190319>
- Ma, X. (2017). A golden era for natural gas development in the Sichuan Basin. *Natural Gas Industry B*, 4(3), 163–173. <https://doi.org/10.1016/j.ngib.2017.08.001>
- Meng, L., McGarr, A., Zhou, L., & Zang, Y. (2019). An investigation of seismicity induced by hydraulic fracturing in the Sichuan Basin of China based on data from a temporary seismic network. *Bulletin of the Seismological Society of America*, 109, 348–357. <https://doi.org/10.1785/0120180310>
- Qian, H., & Tang, R. (1992). Seismo-geological features of the Sichuan Basin. *Earthquake Research in Sichuan*, 3, 13–18.
- Ran, X., Cheng, W., Zhang, Y., Li, J., & Cheng, Y. (2008). Research of the earthquakes induced by water injections in salt mines in Changning, Sichuan. *Earthquake Research in China*, 24(3), 226–234.
- Segall, P., & Lu, S. (2015). Injection-induced seismicity: Poroelastic and earthquake nucleation effects. *Journal of Geophysical Research: Solid Earth*, 120, 5082–5103. <https://doi.org/10.1002/2015JB012060>
- Snoke, J. A. (2003). FOCMEC: FOCAL MECHANISM determinations. In: Lee, W.H.K., Kanamori, H., Jennings, P.C., Kisslinger, C. (Eds.), *International handbook of earthquake and engineering seismology* (Part B: pp. 1629–1630 and accompanying CD) San Diego: Academic Press. [https://doi.org/10.1016/S0074-6142\(03\)80291-7](https://doi.org/10.1016/S0074-6142(03)80291-7)
- Sokos, E., Kiratzi, A., Gallovič, F., Zahradník, J., Serpetsidaki, A., Plicka, V., et al. (2015). Rupture process of the 2014 Cephalonia, Greece, earthquake doublet (M_w 6) as inferred from regional and local seismic data. *Tectonophysics*, 656, 131–141. <https://doi.org/10.1016/j.tecto.2015.06.013>
- Sokos, E., Zahradník, J., Gallovič, F., Serpetsidaki, A., Plicka, V., & Kiratzi, A. (2016). Asperity break after 12 years: The M_w 6.4 2015 Lefkada (Greece) earthquake. *Geophysical Research Letters*, 43, 6137–6145. <https://doi.org/10.1002/2016GL069427>
- Sun, X., Yang, P., & Zhang, Z. (2017). A study of earthquakes induced by water injection in the Changning salt mine area, SW China. *Journal of Asian Earth Sciences*, 136, 102–109. <https://doi.org/10.1016/j.jseaeas.2017.01.030>
- Vackář, J., Burjánek, J., Gallovič, F., Zahradník, J., & Clinton, J. (2017). Bayesian ISOLA: New tool for automated centroid moment tensor inversion. *Geophysical Journal International*, 210(2), 693–705. <https://doi.org/10.1093/gji/ggx158>
- Vavryčuk, V. (2014). Iterative joint inversion for stress and fault orientations from focal mechanisms. *Geophysical Journal International*, 199(1), 69–77. <https://doi.org/10.1093/gji/ggu224>
- Waldhauser, F., & Ellsworth, W. L. (2000). A double-difference earthquake location algorithm: Method and application to the Northern Hayward Fault, California. *Bulletin of the Seismological Society of America*, 90(6), 1353–1368. <https://doi.org/10.1785/0120000006>
- Wang, X. S., Lu, J., Xie, Z. J., & Ai, E. (2015). Focal mechanisms and tectonic stress field in the North-South Seismic Belt of China. *Chinese Journal of Geophysics*, 58(11), 4149–4162. <https://doi.org/10.6038/cjg20151122>
- Yi, G., Long, F., Liang, M., Zhao, M., Wang, S., Gong, Y., et al. (2019). Focal mechanism solutions and seismogenic structure of the 17 June 2019 $M_6.0$ Sichuan Changning earthquake sequence. *Chinese Journal of Geophysics*, 62(9), 3432–3447. <https://doi.org/10.6038/cjg2019N0297>
- Zahradník, J., Čížková, H., Bina, C. R., Sokos, E., Janský, J., Tavera, H., & Carvalho, J. (2017). A recent deep earthquake doublet in light of long-term evolution of Nazca subduction. *Scientific Reports*, 7, 45153. <https://doi.org/10.1038/srep45153>
- Zahradník, J., & Gallovič, F. (2010). Toward understanding slip inversion uncertainty and artifacts. *Journal of Geophysical Research*, 115, B09310. <https://doi.org/10.1029/2010JB007414>
- Zahradník, J., & Plešinger, A. (2010). Toward understanding subtle instrumentation effects associated with weak seismic events in the near field. *Bulletin of the Seismological Society of America*, 100(1), 59–73. <https://doi.org/10.1785/0120090087>
- Zahradník, J., & Sokos, E. (2014). The M_w 7.1 Van, Eastern Turkey, earthquake 2011: Two-point source modelling by iterative deconvolution and non-negative least squares. *Geophysical Journal International*, 196(1), 522–538. <https://doi.org/10.1093/gji/ggt386>
- Zahradník, J., & Sokos, E. (2018). ISOLA code for multiple-point source modeling—Review. In *Moment tensor solutions—A useful tool for seismotectonics* (pp. 1–28). Cham, Switzerland: Springer Natural Hazards. <https://doi.org/10.1007/978-3-319-77359-9>

- Zhao, Z., & Zhang, R. (1987). Primary study of crustal and upper mantle velocity structure of Shichuan Province. *Acta Seismologica Sinica*, 9(2), 154–166.
- Zhu, H., & He, C. (2014). Focal mechanism changing character of earthquake sequence induced by water injection: A case study of Changning sequence, Sichuan Province. *Earth Science - Journal of China University of Geosciences*, 39(12), 1776–1782. <https://doi.org/10.3799/dqkx.2014.161>

1

2

Geophysical Research Letters

3

Supporting Information for

4

**The 2019 Mw 5.7 Changning earthquake, Sichuan Basin, China – a shallow doublet with
different faulting styles**

5

6

Junqing Liu^{1*}, Jiří Zahradník²

7

¹Jilin Earthquake Agency, China Earthquake Administration, Changchun, China

8

²Faculty of Mathematics and Physics, Charles University, Prague, Czech Republic.

9

10

Contents of this file

12

Text S1

Tables S1-S3

Figures S1-S8

16

17 Introduction

18 Here we provide one text detailing the used methods, three tables and eight additional
19 figures illustrating findings of the main text.

20

21 Text S1. Multiple-point source modeling

22 To investigate source process of the 2019 mainshock and the largest aftershocks we use a
23 suite of established waveform-modeling methods, ISOLA software package, continually
24 upgraded since 2003 (Zahradník & Sokos, 2018), and validated on numerous events, e.g.,
25 (Sokos et al., 2016; Zahradník et al., 2017). The methods address both single- and multiple-
26 point source models (MPS). Moment tensor (MT), either full-MT, deviatoric MT, or a double-
27 couple-constrained MT is calculated by least-squares fitting band-pass filtered displacements,
28 accompanied by grid-searching a set of trial source positions. Synthetic waveforms are
29 calculated in 1D velocity models. To assess the MT uncertainty, we draw random samples from
30 the posterior probability density function (PDF) of model parameters. To this goal, a posterior
31 covariance matrix of model parameters is calculated based on a data covariance matrix
32 assumed in its simplest constant-diagonal form. Effect of the uncertain source depth upon
33 PDF, generally non-Gaussian, is accounted for by the recently developed techniques (Halló et
34 al., 2017; Vackář et al., 2017). ISOLA software calculates MPS models with three methods, as
35 follows.

36 (i) **Iterative deconvolution** (Sokos et al., 2015) is a consecutive search for subevents. It can
37 suffer from the general tendency of the method to fit most data by the first retrieved subevent,
38 sub1, thus potentially underestimating the moment ratio sub2/sub1, sub3/sub1, etc., where
39 sub2, sub3 denote the subsequently retrieved subevents, usually characterized by decreasing
40 moments.

41 (ii) **Modified iterative deconvolution** (Zahradník & Gallovič, 2010) makes use of a formal ‘trick’
42 to partially fix the above-mentioned problem in (i). During the consecutive calculation of
43 subevents, their moments are constantly artificially decreased. For example, if the modeling
44 suggests that subevent 1 should have scalar moment m , the code assigns just a fraction of this
45 moment to sub1, e.g., $\frac{1}{4} m$. The same fraction (1/4) is used for all subevents. Naturally, instead
46 of calculating 2 standard subevents, here we calculate 2 x 4 modified subevents. The results of
47 this approach are closer to the slip inversion in finite-source models.

48 (iii) **Joint inversion of source pairs** (Zahradnik & Sokos, 2014). We consider a two-point source
49 model, and assume that a double-couple focal mechanism is known and prescribed for both
50 members of the source pair; these two mechanisms can be unequal. Observed waveforms are
51 jointly inverted for moment-rate time functions of both point sources. Each time function is
52 parameterized with a set of identical, mutually shifted elementary functions (e.g. triangles),
53 and their weights are calculated by the non-negative least squares technique, NNLS (Lawson &
54 Hanson, 1974). Every source pair on a spatial grid is inspected and the output is a suite of the
55 possible source pairs almost equally well-fitting the data. In this way, the uncertainty of the
56 two-point models is estimated.

57

58

59

60

61

62

63

64

65

66

67

68

69

70

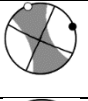


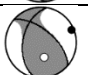
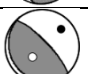
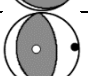
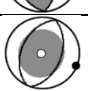
71

72

73

74

75 **Table S1. The 2019 Changning mainshock and its four largest aftershocks.** Except
 76 magnitude M (CENC), the parameters were retrieved in this paper. Latitude and Longitude
 77 come from our relocation by HypoDD method (Waldhauser & Ellsworth, 2000), C-Depth is
 78 centroid depth, s/d/r are strike/dip/rake angles. In each s/d/r cell, the upper and lower
 79 numbers correspond to Figures 4b and 4c, respectively. DC, CLVD and ISO are percentages of
 80 the moment tensor. The constrained mechanisms are denoted with "f" (= fixed). VR is variance
 81 reduction. The frequency range is 0.03-0.06 Hz, except for the case of resolving two subevents
 82 of the mainshock (0.03-0.10 Hz). For uncertainties, see Figure S3. The point-source full-MT
 83 model of the mainshock has a limited meaning because the event was a doublet, consisting of
 84 two DC subevents, and only the P-axis of the point-source model was resolvable.

No.	Date Time (UTC)	Lat (°N) Lon (°E)	C-Depth (km)	M	M _w	M ₀ (10 ¹⁷ Nm)	s/d/r (°)	DC (%)	CLVD (%)	ISO (%)	VR	Focal mech.
1	2019-06-17 14:55:43	28.37 104.88	4.0	6.0	5.74	4.552	114/ 86 /-1 204/89/-176 (limited meaning)	20	-68	-12	0.90	
The strike-slip subevent							116/ 72/ 5 24/86/162	100 f	CLVD of the sum of the two subevents: -46% to -90%			
The thrust-fault subevent (the moment ratio of the TF/SS subevents ~ 0.3-1.2)							170/35/111 325/58/76	100 f				
2	2019-06-17 15:36:01	28.43 104.80	3.0	5.1	5.02	0.380	189/44/137 313/62/55	83	-17	0 f	0.88	
3	2019-06-17 23:34:33	28.38 104.86	3.0	5.3	4.83	0.193	143/13/97 316/77/88	94	+6	0 f	0.79	
4	2019-06-22 14:29:56	28.44 104.78	4.0	5.4	5.16	0.612	172/33/86 357/57/92	97	+3	0 f	0.88	
5	2019-07-04 02:17:58	28.43 104.75	7.0	5.6	5.11	0.516	201/43/90 21/47/90	20	+80	0 f	0.78	

85

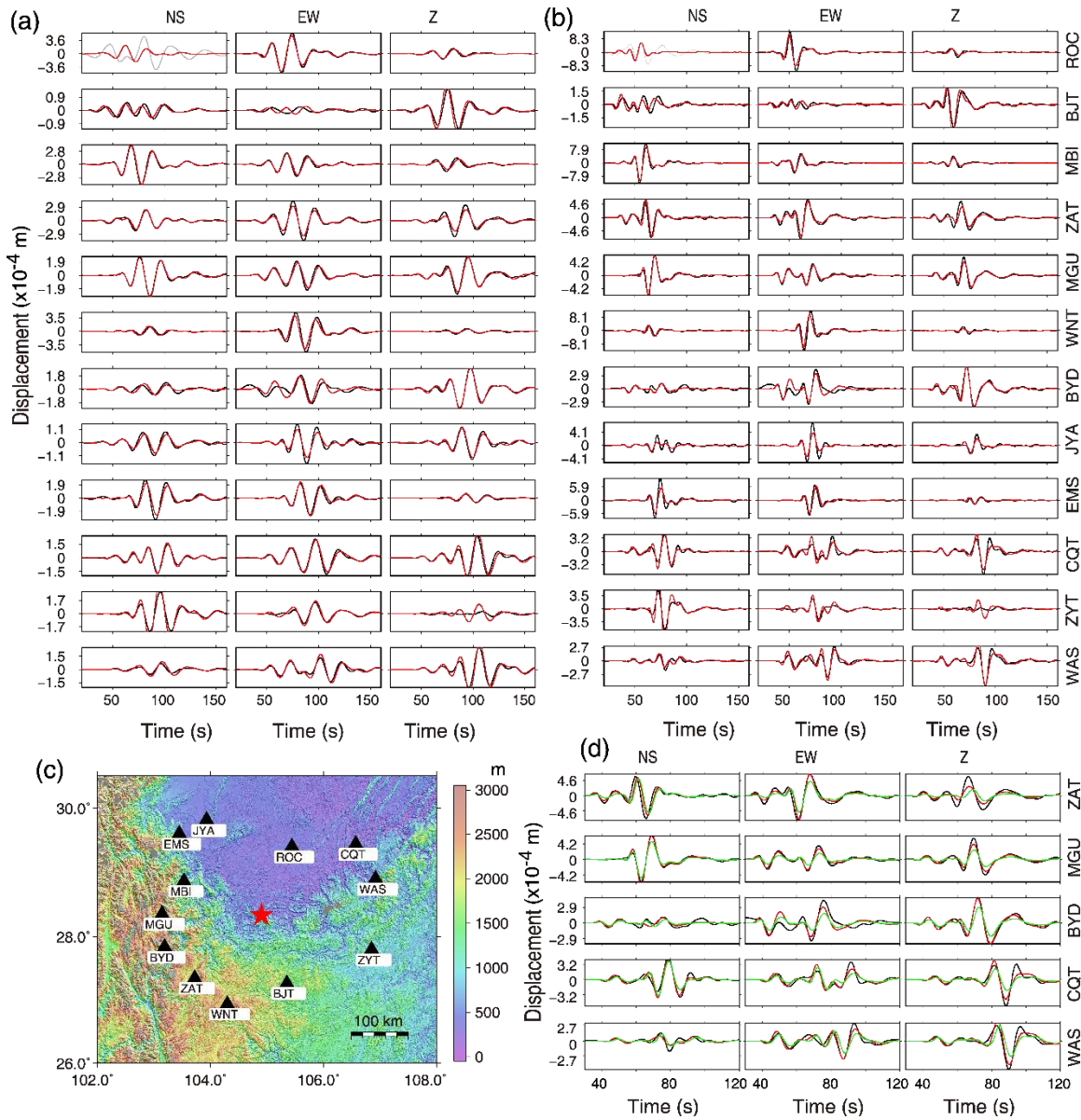
86 **Table S2. The full-MT components of the mainshock.** The single-point source model in
 87 frequency range 0.03-0.06 Hz.

M _w	Depth (km)	M _{rr} / M _{tt} / M _{pp} (10 ¹⁷ Nm)	M _{rt} / M _{rp} / M _{tp} (10 ¹⁷ Nm)
5.74	4.0	1.273/ 1.379/ -4.699	-0.103/ 0.418/ 2.780

88

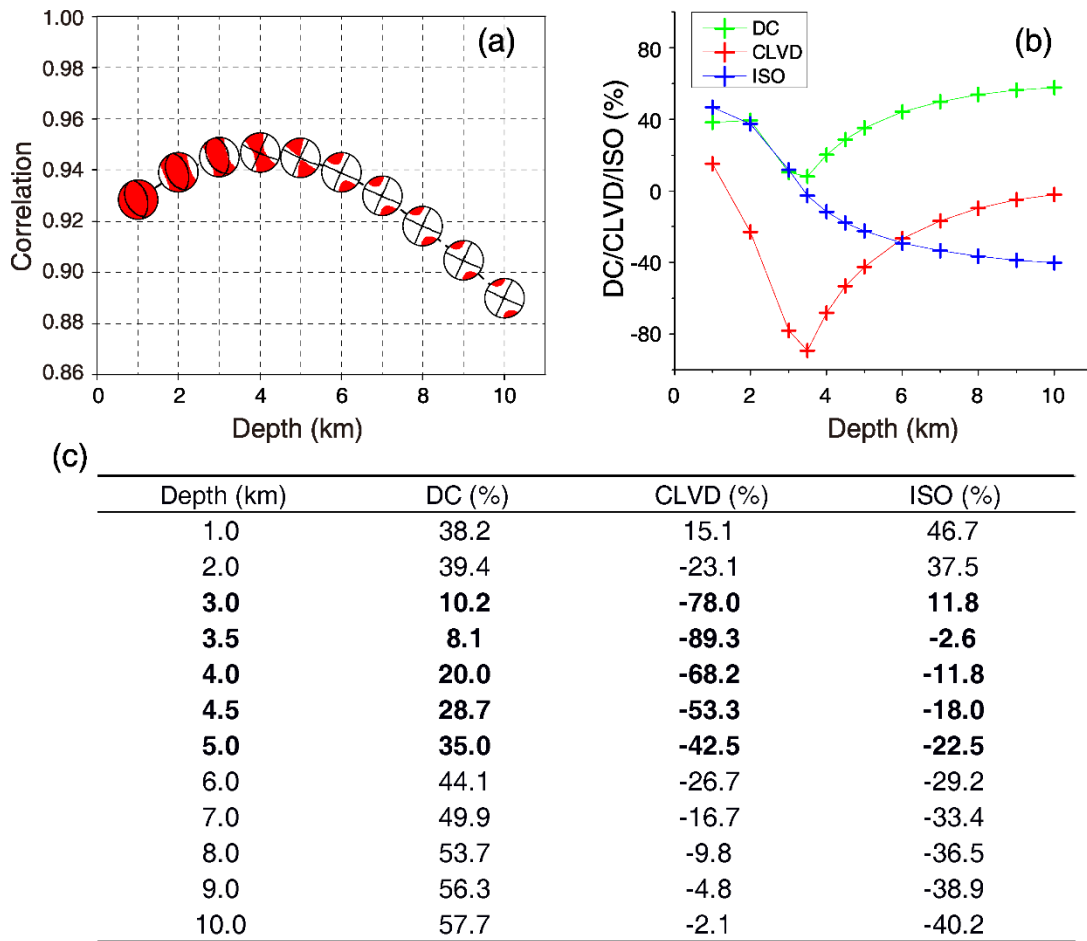
89 **Table S3. The used velocity model.** Shown are the P-wave velocities, V_p (Zhao & Zhang,
 90 1987). The constant P-to-S wave velocity ratio is V_p/V_s = 1.72.

Layer No.	1	2	3	4	5	6	7	8	9	10	11	12	13	14
Depth of the layer top (km)	0.0	0.8	1.6	5.0	10.0	17.7	26.5	28.5	30.5	33.6	37.5	42.5	49.0	61.0
V _p (km/s)	4.60	5.35	5.75	5.87	5.92	6.05	6.25	6.50	6.70	6.80	6.90	6.95	7.05	7.80



91

92 **Figure S1. Waveform inversion of the mainshock.** **a)** The displacement waveform fit for the
 93 *single point-source full-MT model, 0.03-0.06 Hz, VR=0.90.* Observed and synthetic data are
 94 plotted in black and red, respectively. The NS-component of ROC station with an instrumental
 95 disturbance (gray) was removed from the inversion. **b)** The waveform fit for the *single point-*
 96 *source full-MT model, 0.03-0.10 Hz, VR=0.80.* Note that the y-axis differs from panel a). This
 97 model features $s/d/r = 114/68/7$, and $DC=18\%$, $CLVD=-73\%$, $ISO=-9\%$, similar to the mainshock
 98 model in Table S1. **c)** Map of the region and the used broadband stations. The epicenter is
 99 shown by a star. **d)** Comparison of real displacement data (black) with synthetics calculated in
 100 two models: (i) *a two-point DC-constrained model, 0.03-0.10 Hz, consisting of a strike-slip and*
 101 *thrust-fault subevent (red), VR=0.84,* and (ii) *just the strike-slip subevent (green), 0.03-0.10 Hz,*
 102 $VR=0.72$. These models refer to the best-fitting source pair (8, 6) of Figure 3 in the main text.
 103 Shown are all the stations with a visible difference. We emphasize that the preference of the
 104 two-point DC model is not merely due to a slight increase of VR, but because the two-point
 105 model explains the observed first-motion polarities and the apparent non-DC character of the
 106 single-point model.

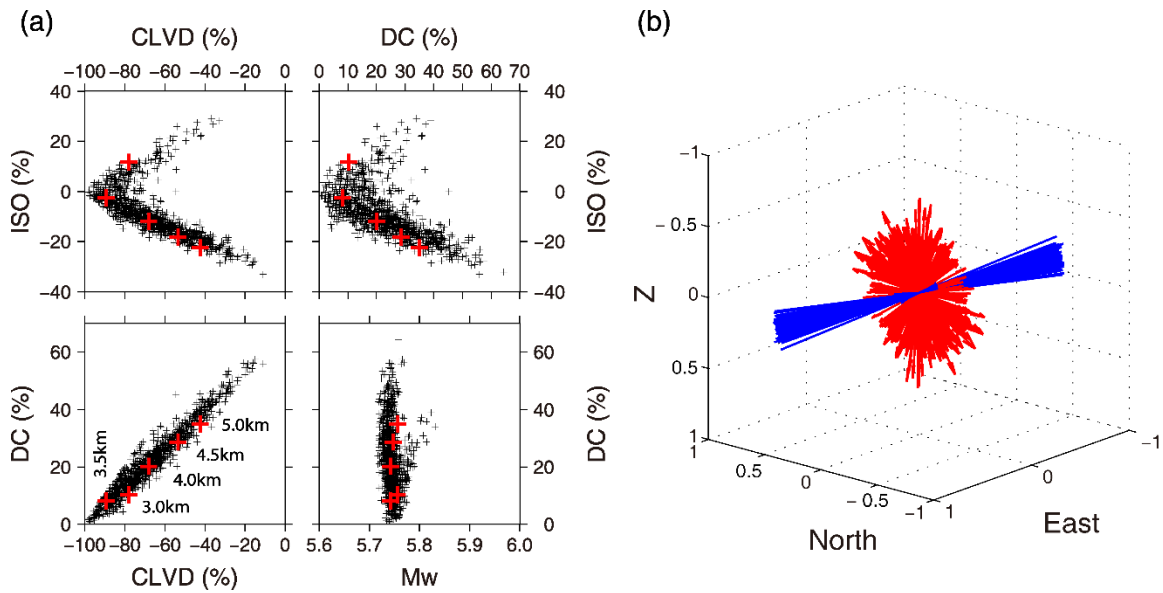


107

108 **Figure S2. Depth variation of the single-point full MT.** **a)** Correlation between real and
 109 synthetic waveforms as a function of depth. The plot is similar to Figure 2a of the main text
 110 (mainshock, 0.03-0.06 Hz), but here the hatching in the focal mechanism diagrams
 111 demonstrates the full moment tensors. **b)** and **c)** The trial depth variation of the DC, CLVD and
 112 ISO content. Highlighted in the table is the depth range of 3-5 km, close to the best fitting
 113 depth (4 km), calculated with a 0.5-km increment. Panel (b) demonstrates that the full-MT
 114 variation with depth is obviously smooth across the DC and CLVD minima and ISO inflection at
 115 ~3.5 km. Contrarily, nodal lines of the focal diagrams in panel (a) change discontinuously,
 116 showing thrust faulting at depths ≤ 3 km, and strike-slip faulting at ≥ 4 km. It is a good
 117 example of how the fault classification and $s/d/r$ angles lose their meaning when the DC
 118 component of an event is small. Note that the “competing” thrust and strike-slip faulting,
 119 observed here, is due to the presence of these two faulting geometries in the mainshock
 120 rupture process (Figure 3 of the main text).

121

122



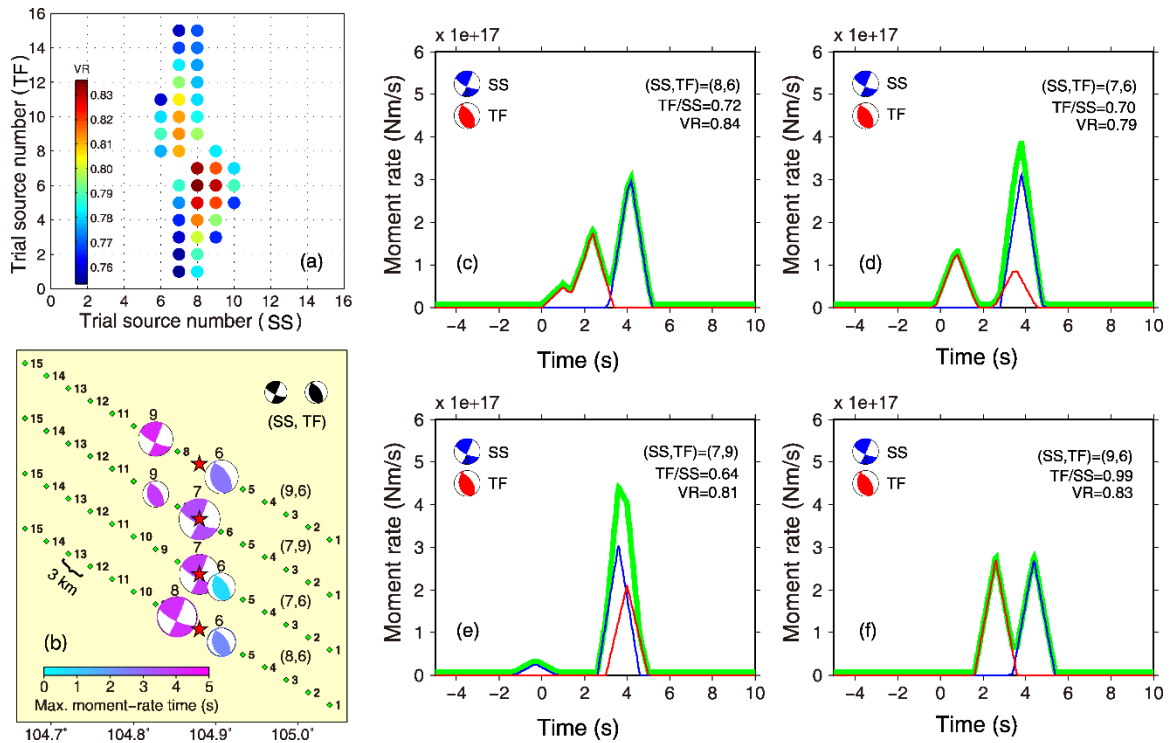
123

124 **Figure S3. Uncertainty of the mainshock point-source full-MT model.** Shown here is the
 125 random sampling of the posterior probability density of model parameters (dots and vectors
 126 in panels (a) and (b), respectively). **a)** The parameter tradeoffs; best-fit solutions are plotted by
 127 red crosses, depth-coded by numbers in the DC-CLVD panel. **b)** The equivalent body-forces of
 128 the deviatoric part of moment tensor. The orientation of the arrows is given by eigenvectors.
 129 Their length scales with eigenvalues; tensions shown in red, compressions in blue. The vertical
 130 axis in panel b) is positive downward. The event is basically a compensated linear vector
 131 dipole whose major axis (blue) is well determined, almost horizontal, while the minor axes (red
 132 vectors, rotating around the blue one) are highly uncertain.

133

134

135



136

137

138

139

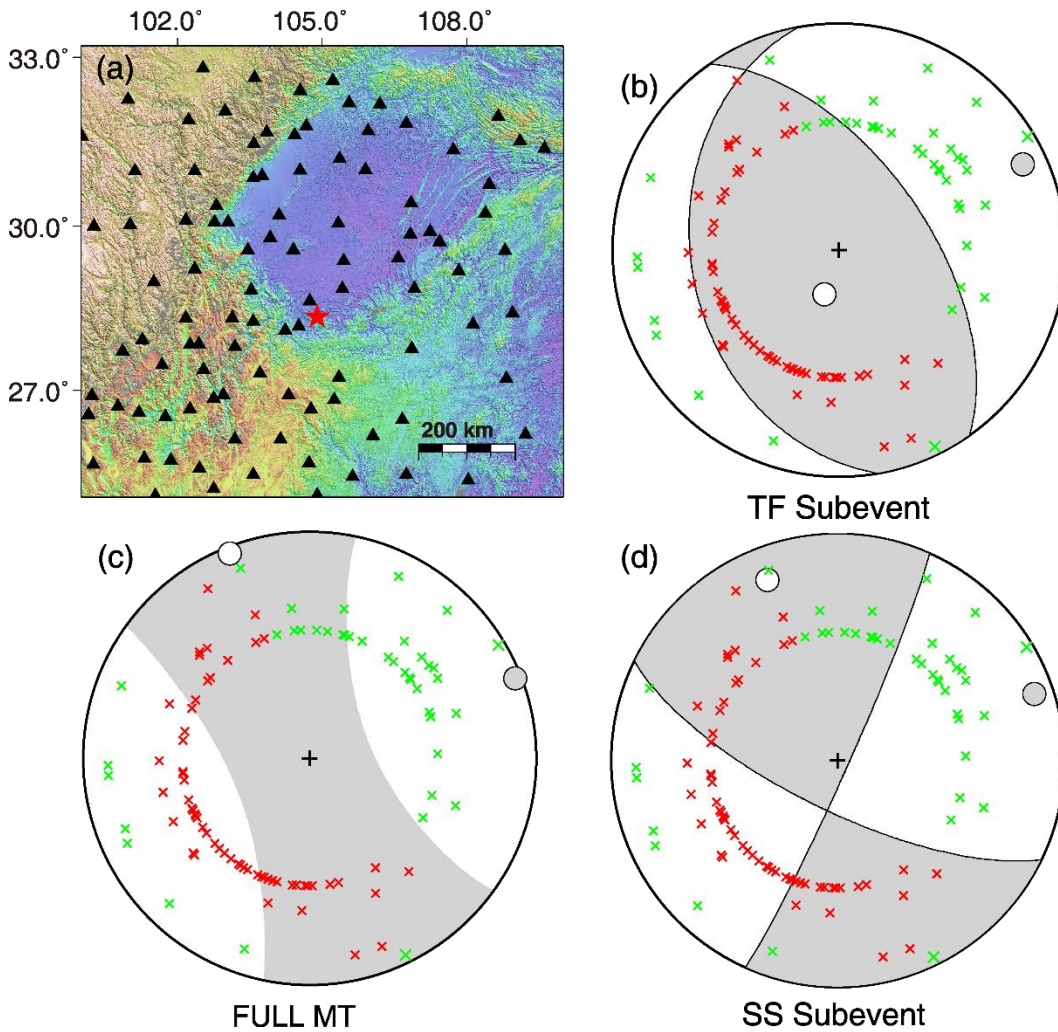
140

141

142

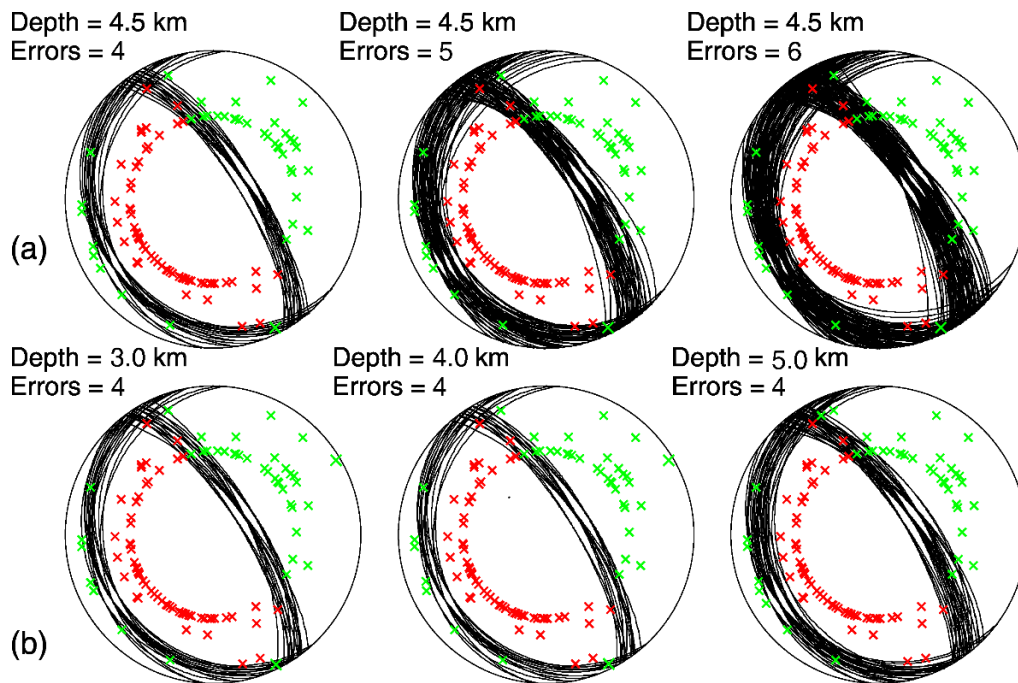
143

Figure S4. The two-point modeling of the mainshock on a horizontal line grid. As in Figure 3c-e of the main text, adding more examples of the moment-rate function, and including moment ratios TF/SS of the two subevents. Each time function is a weighted sum of 60 triangles, spaced by 0.2 s. The total moment of each source pair was constrained. The triangle durations were tentatively chosen to be 2 s, just for good visibility of the subevents. Note that although time shifts can be approximately resolved in the used frequency range < 0.1 Hz, the true duration of every subevent remains undetermined (< 10s).



144

145 **Figure S5. First-motion polarities of the mainshock.** **a)** Used broadband 109 stations
 146 (epicentral distance ~30-600 km). **b)-d)** The observed compressions in red, dilatations in green,
 147 the model compressional sectors shown by shading and the P/T axes plotted as filled/open
 148 circles. Note that the observed polarities strongly disagree both with the full moment tensor
 149 (panel c) and with the strike-slip subevent (panel d). However, data are well fitted with the
 150 thrust-fault subevent (panel b), resulting from the multiple-point models of this paper. It
 151 proves that mainshock nucleated as a thrust faulting although later it continued as a strike slip.
 152 Polarities were projected on the focal sphere with the same velocity model as used in the
 153 waveform inversion (Table S3), assuming a source depth of 4 km.



154

155 **Figure S6. Direct inversion of the first-motion polarities of the mainshock.** The observed
 156 polarities are shown by crosses (compressions in red, dilatations in green). **a)** Using a constant
 157 source depth and a variable number of the allowed polarity errors (see legend). Increasing the
 158 error number, no qualitatively different mechanisms appear, because the polarity constraint is
 159 strong. **b)** Using a constant number of the allowed errors and a variable depth. Code FOCMEC
 160 was used (Snoke, 2003). No solution exists if enabling less than 4 errors. Note that all solutions
 161 are close to the thrust-fault subevent (Figure S5b) that we obtained by waveform inversion
 162 without any polarity pre-constraint. It undoubtedly proves that the mainshock nucleated as a
 163 thrust faulting.

164

165

166

167

168

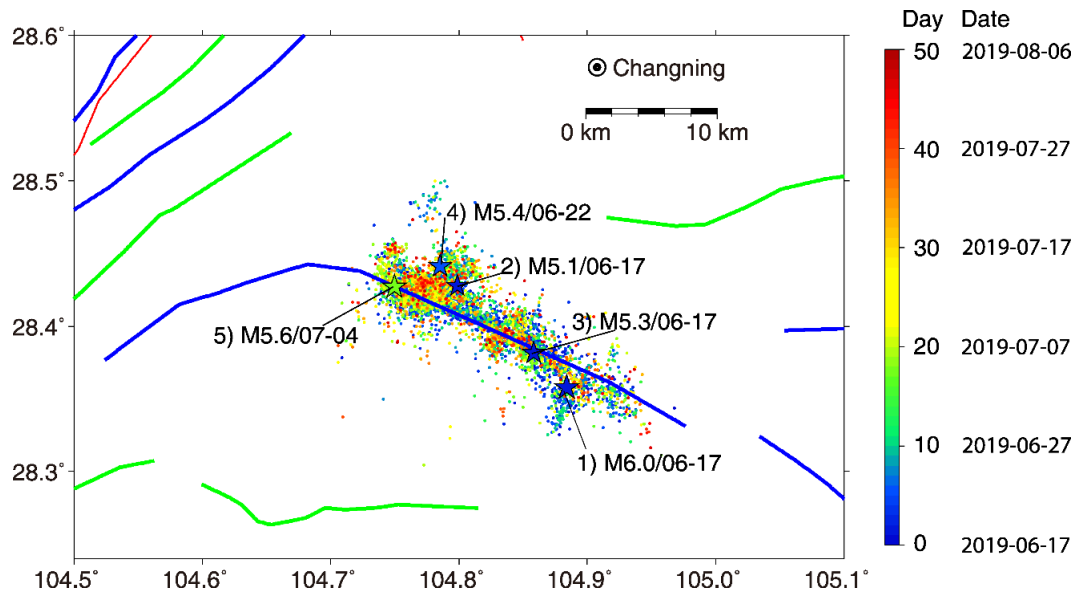
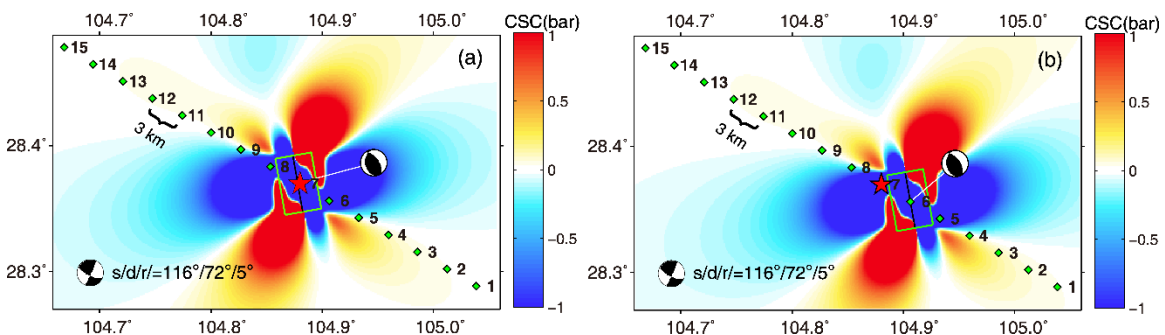


Figure S7. Space-time variation of the aftershock sequence. Shown are 5466 aftershocks of the M6.0 mainshock that occurred between June 17th and August 4th, 2019, relocated by the HypoDD method. The relocation concentrates most of the aftershocks close to the axis of the Changing anticline. The arrangement of the plot is similar to Figure 1b of the main text, but here we add color-coding of the events according to time. However, no systematic migration can be traced.



169 **Figure S8. Coulomb stress change (CSC).** The finite-extent generating TF fault ($s/d/r = 170^\circ$
 170 $/35^\circ /111^\circ$, $M_0 = 2.3e17$ Nm, Depth = 4 km) is placed either in point 7, or 6, see panels (a), (b).
 171 These are two examples of the possible TF position. The receiver fault, assumed to be situated
 172 anywhere in the plotted rectangle, has the SS mechanism, resolved in the multiple-point
 173 modeling of this paper. The assumed friction coefficient is 0.6. With the preferred position of
 174 the SS subevent at point 8 or 9 and the TF subevent possibly situated in hypocenter, point 7,
 175 we should admit that the SS rupture might have been assisted by one of the positive CSC
 176 lobes. For TF in points 6 or 5 its effect upon SS in points 8 or 9 is less likely. Overall, with these
 177 simplified models and their uncertainties, static stress transfer from the initial thrust upon the
 178 subsequent strike-slip is inconclusive.

179
 180
 181
 182
 183

184 **References**

185

186 Halló, M., Asano, K., & Gallovič, F. (2017). Bayesian inference and interpretation of centroid
187 moment tensors of the 2016 Kumamoto earthquake sequence, Kyushu, Japan. *Earth,*
188 *Planets and Space, 69,* 134. <https://doi.org/10.1186/s40623-017-0721-4>

189 Lawson, C., & Hanson, R. (1974). *Solving Least Squares Problems*. Prentice-Hall, Upper Saddle
190 River, N. J.

191 Snoke, J. A. (2003). FOCMEC : FOCal MECHANism determinations. *International Handbook of*
192 *Earthquake and Engineering Seismology* (Vol. 81). Academic Press.
193 [https://doi.org/10.1016/S0074-6142\(03\)80291-7](https://doi.org/10.1016/S0074-6142(03)80291-7)

194 Sokos, E., Kiratzi, A., Gallovič, F., Zahradník, J., Serpetsidaki, A., Plicka, V., Janský, J., Kostelecký, J.,
195 Tselentis, G.-A. (2015). Rupture process of the 2014 Cephalonia, Greece, earthquake
196 doublet (Mw6) as inferred from regional and local seismic data. *Tectonophysics, 656,* 131–
197 141. <https://doi.org/10.1016/j.tecto.2015.06.013>

198 Sokos, E., Zahradník, J., Gallovič, F., Serpetsidaki, A., Plicka, V., & Kiratzi, A. (2016). Asperity break
199 after 12 years: The M w 6.4 2015 Lefkada (Greece) earthquake. *Geophysical Research*
200 *Letters, 43*(12), 6137–6145. <https://doi.org/10.1002/2016GL069427>

201 Vackář, J., Burjánek, J., Gallovič, F., Zahradník, J., & Clinton, J. (2017). Bayesian ISOLA: new tool
202 for automated centroid moment tensor inversion. *Geophysical Journal International,*
203 *210*(2), 693–705. <https://doi.org/10.1093/gji/ggx158>

204 Waldhauser, F., & Ellsworth, W. L. (2000). A Double-difference Earthquake location
205 algorithm: Method and application to the Northern Hayward Fault, California.
206 *Bulletin of the Seismological Society of America, 90*(6), 1353–1368.
207 <https://doi.org/10.1785/0120000006>

208 Zahradník, J., & Sokos, E. (2014). The Mw 7.1 Van, Eastern Turkey, earthquake 2011: two-point
209 source modelling by iterative deconvolution and non-negative least squares. *Geophysical*
210 *Journal International, 196*(1), 522–538. <https://doi.org/10.1093/gji/ggt386>

211 Zahradník, J., & Gallovič, F. (2010). Toward understanding slip inversion uncertainty and
212 artifacts. *Journal of Geophysical Research, 115*(B9), B09310.
213 <https://doi.org/10.1029/2010JB007414>

214 Zahradník, J., & Sokos, E. (2018). ISOLA code for multiple-point source modeling –review. In
215 *Moment Tensor Solutions - A Useful Tool for Seismotectonics* (pp. 1–28). Springer Natural
216 Hazards. <https://doi.org/10.1007/978-3-319-77359-9>

217 Zahradník, J., Čížková, H., Bina, C. R., Sokos, E., Janský, J., Tavera, H., & Carvalho, J. (2017). A
218 recent deep earthquake doublet in light of long-term evolution of Nazca subduction.
219 *Scientific Reports, 7,* 45153. <https://doi.org/10.1038/srep45153>

220 Zhao, Z., & Zhang, R. (1987). Primary study of crustal and upper mantle velocity structure of
221 Shichuan Province. *Acta Seismol. Sin., 9*(2), 154–166.

222

223